

# Transition Metal Oxide Chemistry: Electronic Structure Study of $\text{WO}_3$ , $\text{ReO}_3$ , and $\text{NaWO}_3$

F. Corà,\* M. G. Stachiotti,<sup>†</sup> and C. R. A. Catlow

*Davy-Faraday Research Laboratory, The Royal Institution of Great Britain, 21 Albemarle Street, London W1X 4BS, U.K.*

C. O. Rodriguez

*IFLYSIB, Grupo de Física del Sólido, C.C.565, La Plata (1900), Argentina*

*Received: November 7, 1996; In Final Form: February 28, 1997<sup>®</sup>*

In this paper, we present the results of electronic structure, *ab initio* calculations performed on  $\text{ReO}_3$ ,  $\text{WO}_3$ , and the stoichiometric tungsten bronze  $\text{NaWO}_3$ . We examine the relation between the structural and the electronic properties of the three materials and comment on the solid state chemistry governing the interaction between the transition metal and its oxygen ligands. We show that off-center displacements of the W ion in  $\text{WO}_3$  are driven by the onset of covalent interactions with the nearest oxygen, while the metallic materials  $\text{ReO}_3$  and  $\text{NaWO}_3$  are stable when cubic. In the latter case, antibonding contributions due to the occupation of the conduction band oppose the deformation. The different behavior is justified by examining the band structure of the compounds. The effect of the different number of valence electrons and of the different nature of the transition metal on the electronic distribution in the solid are analyzed. Finally, by comparing the mechanical properties of the three oxides, we show that the antibonding conduction electron makes  $\text{ReO}_3$  very rigid and can suggest an explanation for the pressure-induced phase transition observed for this material.

## I. Introduction

Octahedrally coordinated metal ions ( $\text{MO}_6$ ) are a common structural element in the solid state chemistry of transition metal oxides.<sup>1</sup> Rationalizing the factors that govern the chemical interactions within the elementary  $\text{MO}_6$  building-blocks represents, therefore, a step of fundamental importance in comprehending the behavior of these materials, which have several fields of industrial application arising from their physical and chemical properties, ranging from ferroelectricity to catalytic activity. With this aim, we have recently examined high-valence transition metal oxides using quantum-mechanical calculations, both with Hartree–Fock (HF) ( $\text{WO}_3$ <sup>2</sup> and  $\text{MoO}_3$ <sup>3</sup>) and density functional ( $\text{ReO}_3$ ,  $\text{NaWO}_3$ , and  $\text{WO}_3$ <sup>4</sup>) Hamiltonians. In ref 2, we have characterized cubic and tetragonal  $\text{WO}_3$ , showing that the most important component of the bonding is the electrostatic attraction between metal and oxygens, complemented by a strong, but localized, covalent contribution between the metal and one oxygen ligand. The onset of covalence is the driving force for the symmetry lowering from the cubic to the tetragonal phase. A similar result has been obtained in ref 3 concerning the layered structure of  $\alpha\text{-MoO}_3$ . In ref 3 we also performed a comparison of group VIa oxides with composition  $\text{MO}_3$ , stressing the influence of the degree of covalence in the bonding and of the asymmetrical environment of the oxygens in determining the stable crystal structure. In the present paper, we perform a different comparison, moving horizontally along one row of the periodic table. By analyzing three isostructural compounds:  $\text{WO}_3$ ,  $\text{ReO}_3$ , and the stoichiometric tungsten bronze  $\text{NaWO}_3$  (isoelectronic to  $\text{ReO}_3$ ), we can in fact examine the effect of the different number of valence electrons and of the nature of the transition metal ion on the solid state chemistry.

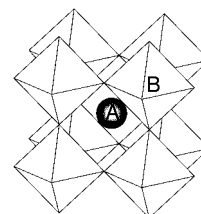


**Figure 1.** Corner-sharing network of  $\text{BO}_6$  octahedra in the perovskite structure  $\text{ABO}_3$ . The dodecahedral interstice of the oxygen sublattice is labeled with A.

The elementary  $\text{MO}_6$  building units in the three materials under investigation form a corner-sharing network, as illustrated in Figure 1; the reference compound for this structure is the naturally occurring mineral Perovskite,  $\text{CaTiO}_3$ . The corner-sharing, perovskite arrangement is a widespread structural type for binary and ternary transition metal oxides: in ternary systems  $\text{ABO}_3$ , the larger cation occupies the 12-fold coordinated sites of the oxygen sublattice (labeled A in Figure 1), while the octahedral network is constructed from corner-sharing of the  $\text{BO}_6$  octahedra of the smaller, B-type cation. In binary compounds, site A is vacant. The availability of empty interstitials in these binary oxides results in a tendency to form insertion compounds; one such material, the tungsten bronze  $\text{NaWO}_3$ , is examined in the present paper. We should emphasize that all the oxygen ions of the perovskite structure are in a 2-fold-coordinated, bridging position between adjacent transition metal sites and are topologically equivalent. We have shown<sup>2,3</sup> that in this case the solid state chemistry is dominated by the interactions between the transition metal and its nearest oxygens.

Experimental evidence shows that in the semiconducting oxide  $\text{WO}_3$  the oxygen sublattice is distorted and the metal ion lies off-center in its coordination octahedron. The solid shows several temperature-induced phase transitions, changing from monoclinic to triclinic, monoclinic, orthorhombic, and tetragonal upon heating, and remains tetragonal up to the melting point.<sup>5</sup> The cubic phase has never been observed.

\* Author to whom correspondence should be addressed (e-mail furio@ri.ac.uk).

<sup>†</sup> Permanent address: Instituto de Física Rosario, Universidad Nacional de Rosario, 27 de Febrero 210 Bis, Rosario (2000), Argentina.

<sup>®</sup> Abstract published in *Advance ACS Abstracts*, April 15, 1997.

In contrast to  $\text{WO}_3$ , the undistorted cubic structure of the conducting oxide  $\text{ReO}_3$  is stable at all temperatures<sup>6</sup> and shows only pressure-induced transitions.<sup>7–10</sup> In a similar way, when metal atoms are introduced in  $\text{WO}_3$  to form the tungsten bronzes  $\text{M}_x\text{WO}_3$ , the relative stability of the undistorted lattice increases, and the cubic phase becomes again stable for large values of  $x$ . In the stoichiometric tungsten bronze  $\text{NaWO}_3$ , the Na atom donates its 3s electron to the conduction band of the solid; the relative stability of the cubic phase can therefore be associated with the number of valence electrons and the occupancy of the conduction band. The importance of this parameter has been investigated<sup>11</sup> with model calculations, employing a simplified and parametrized extended Hückel Hamiltonian. Although the analysis performed in ref 11 is qualitatively correct, the instability of the cubic phase is overestimated with the parameter set used in that study; the authors find, in fact, that for the number of valence electrons corresponding to the stoichiometric bronze the tetragonal distortion involving displacements of the W ion is energetically stable. In our previous *ab initio* calculations on  $\text{ReO}_3$  and  $\text{NaWO}_3$ ,<sup>4</sup> the correct order of stability for the undistorted and distorted phases was, however, predicted. The calculations were also able to reproduce the high-frequency modes of  $\text{ReO}_3$ <sup>4</sup> and are therefore able to describe correctly the energy changes accompanying geometric deformations of the system.

The symmetry reductions shown by  $\text{WO}_3$  are a major feature of the structural chemistry of most perovskite materials and can be taken as a representative case for the whole class. Having identified three chemically very similar materials that display contrasting structural behavior, we consider it necessary to reexamine the problem of the metal–oxygen interaction in perovskite materials with a more accurate method than that used in ref 11 and to perform a chemical analysis of the bonding in the absence of experimentally derived parameters, so as to confirm and improve our understanding of the origin of the deformations.

This paper is organized as follows: In Section II, we give a description of the computational aspects of our study. The results are presented in Section III and IV: structure optimization, electronic structure, and mechanical properties of the cubic materials are in Section III and the relation between electronic structure and lattice stability following the distortions is in Section IV. Finally, Section V contains summary and conclusions.

## II. Computational Details

The electronic structure of the three oxides is calculated using the full-potential linear muffin-tin orbital (FP-LMTO) code developed by Methfessel,<sup>12,13</sup> within the local density approximation (LDA) and the Hedin–Lundqvist exchange-correlation potential. In the FP-LMTO, no shape approximations are made for either the charge density or the potential. The participating states are divided into valence, semicore, and core. Core states are those confined within the muffin-tin (MT) spheres centered on the nuclei; they are treated by solving the radial Schrödinger equation in each iteration (unfrozen core). Semicore states are those associated with very narrow bands that can, however, spill out of the atomic sphere. To provide sufficient variational freedom, it is essential in the method to extend the basis using LMTOs with different localizations. The choice of MT radii was based on the spatial distribution of the self-consistent charge density over the unit cell, which allowed us to attribute charge densities centered at different atoms to their corresponding spheres, leaving only relatively smooth variations of the charge density over the interstitial region. The only exception is Na, whose sphere is enlarged in order to

**TABLE 1: Basis Set and MT Sphere Radii Used in the Calculation**

atom	$\kappa^2 = -0.01R_y$	$\kappa^2 = -1.0R_y$	$\kappa^2 = -2.3R_y$	$R_{\text{MT}}$ (au)
Re	6s 5p 5d 4f	6s 5p 5d	6s 5p	1.85
W	6s 5p 5d 4f	6s 5p 5d	6s 5p	1.85
O	2s 2p 3d	2s 2p	2s 2p	1.47
Na	3s 2p	3s		3.2

**TABLE 2: Lattice Parameter (Å) and Calculated Bulk Modulus (GPa) for the Optimized Cubic Structures of  $\text{ReO}_3$ ,  $\text{WO}_3$ , and  $\text{NaWO}_3$**

	FP-LMTO	HF <sup>a</sup>	HF + correl. <sup>a</sup>	exptl
Lattice Parameter (Å)				
$\text{ReO}_3$	3.71	3.70	3.65	3.75
$\text{WO}_3$	3.78	3.76	3.72	
$\text{NaWO}_3$	3.83	3.85	3.79	3.85
Bulk Modulus (GPa)				
$\text{ReO}_3$	304	282	320	
$\text{WO}_3$	254	257	281	
$\text{NaWO}_3$	241	233	263	

<sup>a</sup> Hartree–Fock calculations are from refs 2, 17, and 18.

include some surrounding interstitial space. In the binary oxides, empty spheres (of radius  $R_{\text{MT}} = 3.2$  au) were added at the dodecahedral sites in order to achieve better space filling. The resulting packing parameter ( $V_{\text{MT}}/V_{\text{total}}$ ) was around 58%.

As is customary for an LMTO approach, the basis for the wave function consists of atom-centered Hankel functions which are augmented by numerical solutions of the radial Schrödinger equation within the nonoverlapping atomic spheres. In the interstitial region, the charge density is represented by fitting a linear combination of Hankel functions to the values and slopes on the sphere boundaries. The envelope function decays as  $e^{-\kappa r}$ , where  $-\kappa^2$  is the kinetic energy of the Hankel function.

The FP-LMTO calculations were performed employing a basis set (presented in Table 1) that was found to be optimal for describing the band structure of these oxides; a similar procedure was used in the study of the closely related ferroelectric perovskite  $\text{KTaO}_3$ .<sup>14</sup> In addition, Re 5s and W 5s states have been explicitly included in the separate semicore panel.

The Brillouin zone integrations were carried out by the tetrahedron method using 35 irreducible k-points (corresponding to  $8 \times 8 \times 8$  regular divisions along the  $k_x$ ,  $k_y$ , and  $k_z$  axes, respectively).

## III. Electronic Structure in the Cubic Phase: the Effect of the Transition Metal on the Structural Chemistry

In this section, we examine the cubic phase of  $\text{ReO}_3$ ,  $\text{WO}_3$ , and  $\text{NaWO}_3$ , to understand the role played by the nature of the transition metal ion on the structural chemistry. Deformations from the cubic structure are examined in Section IV.

**A. Structure Optimization.** Prior to analyzing the electronic properties, we have optimized the structure of the three materials under investigation. For a cubic phase this is a straightforward procedure: since the structure does not contain internal degrees of freedom, the change consists in an isotropic compression or expansion of the unit cell, and corresponds to calculating the total energy as a function of the lattice parameter  $a$ . The results are shown in Table 2. The equilibrium lattice constants for  $\text{ReO}_3$  and cubic  $\text{WO}_3$  are calculated as 3.71 Å and 3.78 Å, respectively; the bronze  $\text{NaWO}_3$  is more expanded ( $a = 3.83$  Å) because of the steric effect of the extra atom in the dodecahedral interstices (see Figure 1). For  $\text{ReO}_3$ , the minimum of the total energy as a function of volume occurs at  $V/V_{\text{exptl}} = 0.969$ , a difference that is typical of DFT calculations using the local density approximation. As cubic  $\text{WO}_3$  has never been observed experimentally, we compare our results with

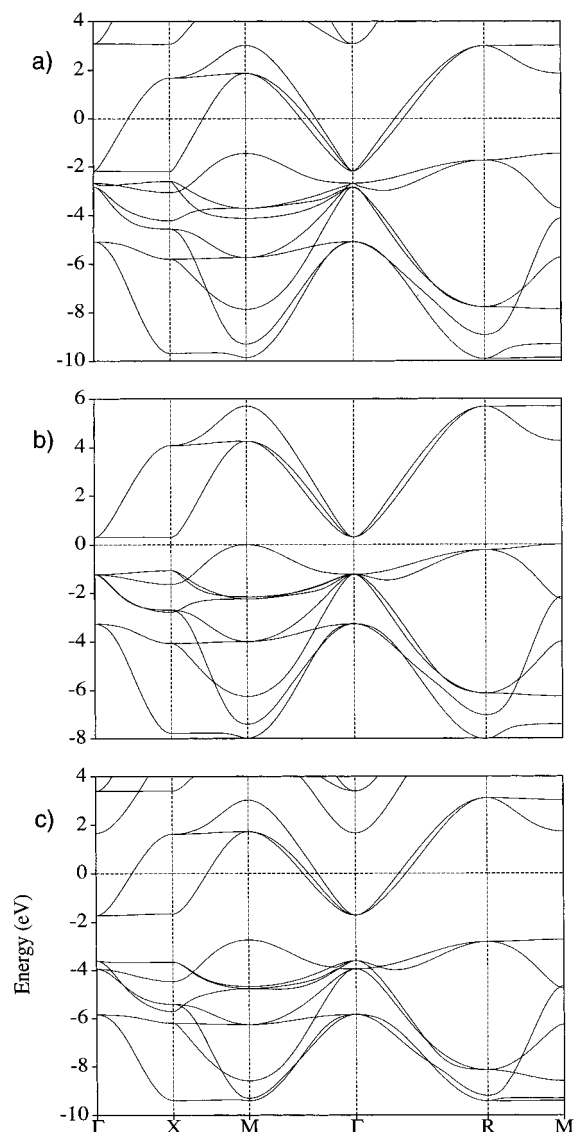


**Figure 2.** Band structures of  $\text{ReO}_3$  (a),  $\text{WO}_3$  (b), and  $\text{NaWO}_3$  (c) along a path in reciprocal space typical for the cubic structure. The zero of energy has been chosen as coincident with the Fermi level of the materials.

those from Hartree–Fock calculations<sup>2</sup> and note the good agreement (within 1–2%) in the equilibrium lattice constants obtained with the two techniques; the LDA values are slightly greater than those obtained at pure HF level, or correcting the HF results for electronic correlation with a generalized gradient density functional.<sup>15</sup> Finally, for  $\text{NaWO}_3$  we can compare the equilibrium lattice constant with the estimate given by the empirical formula  $a = 3.7899 + 0.0601x$  (in Å) (valid for  $\text{Na}_x\text{WO}_3$  when  $x > 0.75$ <sup>16</sup>) for  $x = 1$ . HF results for  $\text{ReO}_3$ <sup>17</sup> and for  $\text{NaWO}_3$ ,<sup>18</sup> obtained with the same technique and computational parameters described in ref 2, are also reported in Table 2 and confirm the good agreement of the two techniques in calculating the lattice spacing of these compounds.

**B. Band Structure.** Let us now analyze the electron density in the three oxides: in Figure 2, we report the three band structures, calculated at the equilibrium lattice parameters, along a path in reciprocal space typical for cubic materials (we note that both here and in the following figures, the zero of energy is chosen as coincident with the Fermi level of the solid). We see that the three band structures are topologically very similar, as expected from the similar chemical nature of the transition metals involved. Because of the different number of valence electrons per unit cell, however, the three oxides have completely different electrical properties; the conduction band is

empty in  $\text{WO}_3$  and half-filled in  $\text{ReO}_3$  and  $\text{NaWO}_3$ , making the latter two materials metallic conductors, while  $\text{WO}_3$  is a nonconductor.

Previous studies have been reported on the band structure of these oxides. It is therefore useful to start our analysis with a comparison of our findings with these previous results, in order to assess the accuracy of our and previous calculations. Cubic  $\text{ReO}_3$  was studied using semiempirical calculations by Mattheiss,<sup>19</sup> using the tight-binding (TB) Slater–Koster LCAO scheme; the TB parameters were adjusted to fit optical and Fermi surface data. The general features of our band structure are not greatly different from the earlier calculation;<sup>19</sup> there are, however, appreciable differences in band widths and gaps. In our calculation, the widths of the conduction and valence bands are approximately 5 and 8.4 eV, respectively. These values are greater than the 4 and 6.5 eV obtained in ref 19. The oxygen 2s bands are centered at  $\sim 20$  eV below the Fermi level and have a band width of 2.8 eV. In the TB band structure there is a gap between the conduction and valence bands, unlike our calculations where the top of the valence band at the M point overlaps the energy range of the conduction band, although this could be a consequence of the DFT–LDA approximation, which is known to underestimate band gaps.<sup>20</sup> Finally, in our calculations the conduction band is split along the  $\Gamma$ –R and  $\Gamma$ –M directions, a feature that is particularly important in determining the Fermi surface<sup>4</sup> and that influences the conductivity of the solid. To obtain similar splittings in the TB calculation it was necessary to introduce a spin-orbit parameter, which was determined by comparison between the theoretical and experimental Fermi surface areas. This effect arises in our calculation without including spin-orbit coupling; it is a result of the band mixing caused by next-nearest neighbor interactions, neglected in the TB calculations.

The band structure of  $\text{WO}_3$  calculated in this study compares favorably with the HF results;<sup>2</sup> in both cases the top of the valence band is at the M point, and the bottom of the conduction band along the  $\Gamma$ –X direction. The difference in valence band width of 8.0 eV in this DFT study and 9.5 eV in the HF calculations reflects the errors typical of the two Hamiltonians employed, as does the main band gap of 0.3 eV (DFT) and 7.7 eV (HF). Despite the large difference, the calculated gap value falls within the range typical of semiconducting materials in the respective techniques<sup>20,21</sup> and is consistent with the experimental value of 2.6 eV.<sup>22</sup> The same splitting of levels in the conduction band previously noted for  $\text{ReO}_3$  is present in  $\text{WO}_3$  in both DFT and HF solutions.

Regarding the bronze  $\text{NaWO}_3$ , an early study was performed by Christensen and Mackintosh<sup>23</sup> within the atomic sphere approximation (LMTO–ASA), a poorer approximation than the one employed in our study, but using the same DFT–LDA Hamiltonian; results for the band structure are not strongly affected by the different approximations of the two studies. The valence band width in the bronze is 7.1 eV, considerably lower than in the binary oxides  $\text{ReO}_3$  and  $\text{WO}_3$ .

**C. Chemical Bonding.** Let us now examine the atomic contributions to the single bands. To do so, we make use of a projection of the band structure onto the basis set associated with the muffin-tin atomic spheres. The components obtained with the previous operation are reported in Figure 3, along the  $\Gamma$ –X–M direction of the reciprocal space; the width of the shaded area is proportional to the indicated atomic contribution to each band. The qualitative result is comparable for the three materials, and in Figure 3 we report only the case of  $\text{ReO}_3$ . In a muffin-tin-based theoretical framework, as mentioned in Section II, the electronic distribution of the solid is expanded in terms of two different basis functions: in the near-nuclear

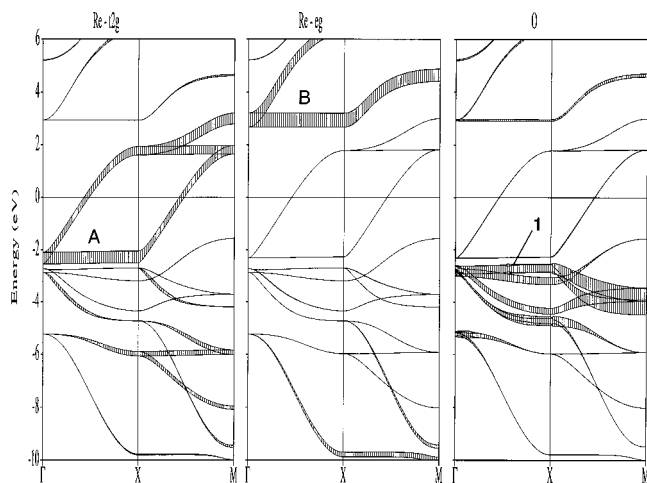


**Figure 3.** Projected band structure of  $\text{ReO}_3$  indicating the atomic contributions to each band along the  $\Gamma$ -X-M directions. Bands labeled with A and B (in the conduction band) and 1 (in the valence band) are pure  $\text{Re}(d_{t_{2g}})$ , pure  $\text{Re}(d_{e_g})$ , and pure  $\text{O}(2p)$  states, respectively.

region, electrons are described by atomic-like orbitals, localized within the atomic MT spheres. A one to one correspondence is in this way established between atomic sites of the structure and basis functions, and the charge that the latter describe can be unambiguously attributed to single atomic species. Outside of the MT region, the basis set is formed by delocalized Hankel functions; no clear correspondence can be established in this case between basis functions and lattice sites. The projection technique provides the value of the atomic charges within the MT spheres only, and the projected atomic values are partial contributions. Bearing this in mind, in the following discussion we make only a qualitative use of these values, to highlight whether atomic orbitals of different symmetry and belonging to metal and oxygens contribute to a specified band or not. Quantitative analyses based on the projected values, for instance, to determine the net charges in the crystal, can provide wrong and misleading results. For instance, in ref 23, the projection technique results in the unphysical value of the net charge on the Na atoms that are described as having a negative ionic charge of  $-1.05 |e|$ .

The projected band structure of Figure 3 is nonetheless needed to highlight the contributions from the Re and oxygen orbitals to each band: we note that the valence band is formed mainly by O 2p states (and is composed of 9 levels, 3 from each of the 3 oxygens of the formula unit), although they are hybridized with the Re 5d orbitals. The conduction band has a dominant contribution from the Re 5d- $t_{2g}$  orbitals (3 levels), while the Re 5d- $e_g$  orbitals (2 levels) lie at a higher energy. This trend in the band composition closely resembles that obtained for cubic  $\text{WO}_3$  in ref 2. The same arguments advanced there apply here: mixing of oxygen and metal states occurs in both valence and conduction bands, but we can clearly distinguish a dominant contribution from the oxygens in the valence band and from the metal in the conduction band (partly occupied in the case of the metallic  $\text{ReO}_3$  and  $\text{NaWO}_3$ ). The hybridization pattern can be interpreted, in more classical terms, as a backdonation of electrons from the filled  $\text{O}^{2-}$  (2p) atomic orbitals to the empty 5d orbitals on the metal.

It is important to note the presence of three levels along the  $\Gamma$ -X direction, denoted in Figure 3 with the labels "A" and "B" (in the conduction band) and "1" (in the valence band), which are pure  $\text{Re}(t_{2g})$ , pure  $\text{Re}(e_g)$ , and pure  $\text{O}(2p)$  levels respectively, with no mixing of orbitals. These levels were denoted as *superdegenerate* in the extended Hückel calculations.<sup>11</sup> We can assume that the relative energy of levels A, B, and 1 marks the zero energy of the metal  $t_{2g}$  and  $e_g$  and oxygen 2p levels in the

crystal field, and in the following discussion we can measure the splitting of levels following the metal-oxygen interaction, relative to this zero. Levels equivalent to A, B, and 1 are present in  $\text{WO}_3$  and  $\text{NaWO}_3$ , as well; as discussed in ref 11, they arise from symmetry requirements of the solution. The difference in energy between bands A and 1 ( $\Delta E_1 = E(A) - E(1)$ ) can be interpreted on purely electrostatic grounds; its value is  $\Delta E_1 = 0.40, 1.35$ , and  $1.85$  eV, respectively, in  $\text{ReO}_3$ ,  $\text{WO}_3$ , and  $\text{NaWO}_3$ . The differences are due to the different crystal field (Coulombic forces) acting on oxygen and metal ions: moving from  $\text{ReO}_3$  to  $\text{WO}_3$ , the main difference is the decrease of the total nuclear charge of the transition metal ion; this change affects the atomic orbitals centered on W more than those belonging to the oxygens, because the former are closer to the nuclear charge. This contribution accounts for the increase in  $\Delta E_1$  in  $\text{WO}_3$  compared to  $\text{ReO}_3$ . Moving from  $\text{WO}_3$  to  $\text{NaWO}_3$ , we add a +1 cation in the dodecahedral interstices (A in Figure 1); the inserted ions are closer to the oxygens ( $2.71 \text{ \AA}$ ) than to the W ions ( $3.32 \text{ \AA}$ ). All the one-electron energy levels are stabilized by the positive charge added, but oxygen levels are stabilized more strongly due to the closer proximity to the  $\text{Na}^+$  ions. On passing from  $\text{WO}_3$  to  $\text{NaWO}_3$ , therefore, the splitting  $\Delta E_1$  increases. The changes are due only to the different Coulombic field.

To understand the effect of the surrounding solid on the energy levels, we start from an ideal ionic solution, corresponding to formal ions:  $\text{O}^{2-}$  with filled O 2p orbitals (valence band) and metal with empty d- $t_{2g}$  (lower part of the conduction band) and d- $e_g$  orbitals (upper part of the conduction band). As in classical ligand field theory, the metal d orbitals are split by the octahedral field of the oxygen ligands, with the  $t_{2g}$  levels at lower energy; this explains the energy difference between the levels A and B in the conduction band. In a similar way, the O(2p) levels can be divided into  $\sigma$  (i.e., the 2p AO pointing directly toward the two nearest metals) and  $\pi$  (the set of the two 2p AOs perpendicular to the M-O-M direction). The  $\sigma$  orbitals point directly toward the positive charge of the cations and are at lower energy than the oxygen  $\pi$  orbitals. As a second step, we allow the mixing of the filled O 2p AOs with the vacant metal d AOs. The resulting hybridization causes a broadening of the atomic levels into bands; the metal-oxygen interaction is bonding in the valence band (levels are stabilized in the hybridization and shifted toward lower energies) and antibonding in the conduction band (levels are destabilized and shifted to higher energies). The stabilization of the valence band levels arising from this interaction is proportional to the overlap of the metal and oxygen orbitals involved; this is maximum for the orbitals of  $\sigma$  symmetry that point directly toward one another. According to the previous analysis, we can therefore speak of both  $\sigma$  and  $\pi$  contributions to the bonding in the solid state chemistry of the compounds. In the conduction band, the metal energy levels are destabilized by the antibonding combination with the oxygen orbitals, in a similar way, but with opposite sign, with respect to the valence band. The destabilization of the  $e_g$  sub-band is therefore larger than the destabilization of the  $t_{2g}$  band.

For completeness, in Figure 4 we report the total density of states (DOS). We will make use of it in Section IV to derive the total one-electron energy of the system. It is interesting to note in the DOS that, in all three materials examined, the top of the valence band is formed by pure oxygen states; this is a common feature of several oxides,<sup>2-4,18</sup> which in ref 3 we have attributed to the unshared oxygen electron pairs.

**D. Electronic Charge Density.** The electronic charge density in  $\text{ReO}_3$  was investigated experimentally by X-ray structural analysis:<sup>24</sup> an anisotropic charge distribution was

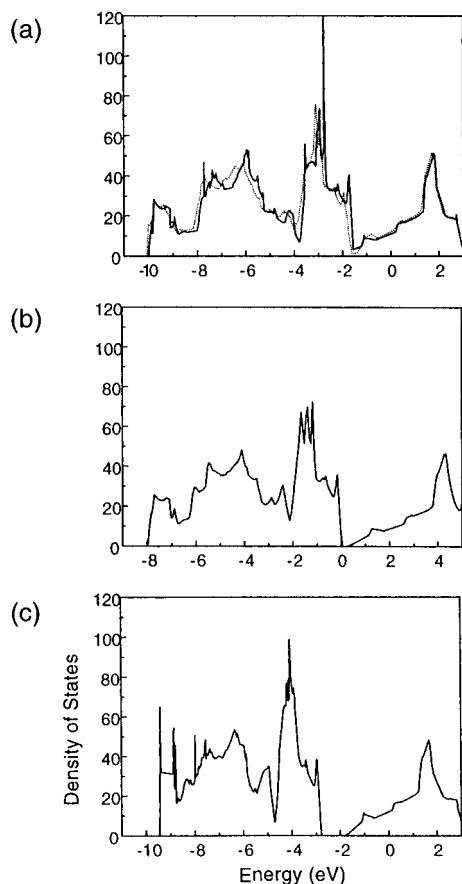


**Figure 4.** Total DOS for (a)  $\text{ReO}_3$ , (b)  $\text{WO}_3$ , and (c)  $\text{NaWO}_3$ . In the  $\text{ReO}_3$  plot, the continuous line refers to the cubic structure and the dashed line to the distorted system (Re displaced by 3%  $a_0$  along the [001] direction).

found around the Re atom, which was attributed to the  $\pi$  bond formed by Re  $5d(t_{2g})$  and O  $2p$  electrons, an effect which we explain by the analysis of the bonding given above. The experimental data also indicated that the thermal vibrations of the oxygen atoms were remarkably anisotropic at all temperatures: the amplitude of the oxygen vibration toward Re is much smaller than in the perpendicular direction toward the empty spaces of the structure. These are structural requirements of the solution, corresponding to structural features of the solid, as evident in Figure 5a, where we show the calculated valence charge density of  $\text{ReO}_3$  in the (001) plane. The metal and oxygen positions marked in Figure 5a serve as a reference for Figure 5b,c.

The total electronic charge densities for cubic  $\text{WO}_3$  and  $\text{NaWO}_3$  do not show appreciable differences from the one shown in Figure 5a for  $\text{ReO}_3$ . Since in our method of calculation we cannot use the quantum-mechanical self-consistent solution for the charge density to evaluate the net atomic charges in the crystal, in the following discussion we make use of a pictorial description of the electronic redistribution: to highlight the changes that occur in the three oxides, we have compared the valence density of the two metals with that obtained for  $\text{WO}_3$ . Figure 5b reports the difference between  $\text{ReO}_3$  and  $\text{WO}_3$  in the (100) plane. In both cases we have employed the equilibrium lattice parameter of  $\text{ReO}_3$  (3.71 Å). Given the similarity in the band structures, this procedure can be considered as equivalent to integrating the density of the half-filled conduction band in  $\text{ReO}_3$  (showing also the effect of the different potential in the two crystals); this map therefore shows the distribution of the electron responsible for the metallic conductivity of  $\text{ReO}_3$ . The corresponding difference density map for  $\text{NaWO}_3$  is shown in Figure 5c. We first note that in  $\text{ReO}_3$  the conduction electron

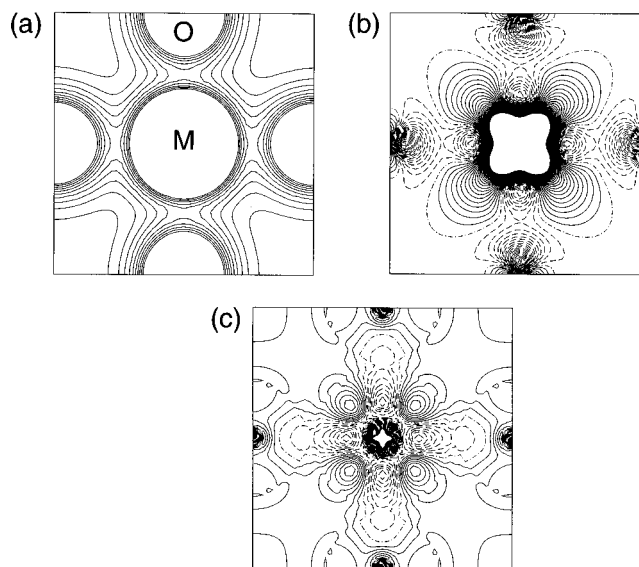


**Figure 5.** Valence charge density of  $\text{ReO}_3$  (a) and difference between the self-consistent charge density for the metals and  $\text{WO}_3$  in the (100) plane: (b)  $\text{ReO}_3$ ; (c)  $\text{NaWO}_3$ . Continuous, dashed, and dot-dashed lines correspond to positive, negative, and zero densities, respectively; the interval between consecutive isodensity lines is 0.0015 au ( $e/\text{Bohr}^3$ ).

is well localized in a  $t_{2g}$  orbital on the metal center, while this is not the case in the bronze, where the electron is more delocalized, with important contributions over the whole structure and in particular in the interstitial region. The plane selected in Figure 5 does not contain the Na ions; the increased density at the corners of Figure 5c, with respect to Figure 5b, is not therefore directly associated with the Na nuclear region. The  $\text{Na}^+$  cations modify the crystal field in the bronze and increase the polarization of the oxygen ions in the direction perpendicular to  $\text{W}-\text{O}$ , as can be noted in Figure 5c. In both cases ( $\text{NaWO}_3$  and  $\text{ReO}_3$ ), we observe a depopulation of the metal  $e_g$  orbital. This effect is not a direct consequence of the extra electron in the unit cell; examining the band structures of Figure 3, in fact, we note that the electron occupies a level of pure  $t_{2g}$  character. The  $e_g$  depopulation must therefore be linked indirectly to the added electron. Two distinct electronic effects appear to be responsible for the depletion of the  $e_g$  level: the extra electron decreases the net charge of the transition metal ion, and the neighboring oxygens are less polarized. In more classical language, this is equivalent to saying that the electron affinity of the transition metal ion is decreased by reducing its net charge. The oxygen orbitals that are most affected by the change are the  $2p$  of  $\sigma$  symmetry that point directly toward the metal and are closer to the effective ionic charge. This causes a destabilization, and subsequent depopulation, of  $\sigma$  levels, whose component on the metal are the  $e_g$  orbitals. Moreover, the antibonding between metal and oxygens due to the population of the  $t_{2g}$  level deforms the oxygens and has an indirect effect on the metal. In the maps of Figure 5b,c, we see that the oxygens “reorient” their electrons toward the region of space perpendicular to the  $\text{M}-\text{O}-\text{M}$  direction. The better exploitation of the empty spaces of the perovskite structure decreases the two-body repulsion in the solid and causes the depopulation of the metal–oxygen internuclear region. The above effect is more pronounced in  $\text{NaWO}_3$  than in  $\text{ReO}_3$  because the  $\text{Na}^+$  ions modify the crystal field and contribute to the “reorientation” of the O  $2p$  electrons.

The net effect of the extra electron on the chemical interaction, therefore, is to cause a decrease of the metal–oxygen bonding strength in the two metals with respect to  $\text{WO}_3$ . In particular, the strength of the  $\pi$  bonding is decreased by populating the antibonding  $t_{2g}$  orbital; it also decreases the

strength of the  $\sigma$  bonding via the depopulation of the  $e_g$  levels. We cannot quantify the degree of covalence in our method, due to the limitations of the projection technique; we know from the HF results<sup>2</sup> that this is only a minor effect in the solid state chemistry of cubic  $\text{WO}_3$  when compared with the Coulombic field.

**E. Mechanical Properties.** A final, and interesting, comparison for the three oxides arises from the analysis of their mechanical properties. We have evaluated the bulk modulus ( $B$ ) using several equations of state proposed in the literature;<sup>25–31</sup> they all agree within 1%. The  $B$  values obtained are reported in Table 2; comparisons with HF values are reported.<sup>2,17,18</sup> The agreement is excellent; the bulk modulus is in fact a second derivative of the total energy of the solid and is therefore very sensitive to small differences in the self-consistent solution. The consistence of HF and DFT results confirms the accuracy of our calculations.

Comparing the bulk moduli for the three oxides under investigation is particularly instructive in understanding the effect played by electrons and interstitial ions on the mechanical properties of the materials. The series  $\text{WO}_3 \rightarrow \text{ReO}_3 \rightarrow \text{NaWO}_3$  can be thought in terms of the subsequent addition of one electron and one interstitial sodium ion to the  $\text{WO}_3$  structure. From the results of Table 2 we see that the extra electron present in  $\text{ReO}_3$  increases considerably the rigidity of the material. The electron occupies an orbital that is antibonding between Re and oxygens, and its energy increases when compressing the material by an amount proportional to the increase of overlap between the metal and oxygen AOs involved. As to the effect of the interstitial Na ion, we might expect a pronounced increase in the resistance opposed by the material to isotropic compressions, parallel to the increased space occupation, in a way comparable to a mechanical hardening of the structure. According to our calculations, the situation is exactly the opposite: the increase in lattice spacing caused by the interstitial ion ( $a = 3.83$  Å in  $\text{NaWO}_3$ ;  $a = 3.71$  Å in the isoelectronic  $\text{ReO}_3$ ) decreases the transition metal–oxygen and the oxygen–oxygen two-body repulsion. In compressing the solid, short-range repulsions are therefore less important and the bulk modulus correspondingly lower.

The very high bulk modulus calculated for  $\text{ReO}_3$  suggests an explanation of the pressure-induced phase transitions that characterize this oxide.<sup>7–10</sup> In our calculations, we have examined only isotropic compressions of the solid, that involve a change of the M–O distance; in these conditions, by increasing the applied pressure, the stress acting along the Re–O direction is very high and can be relieved by diverting it toward the oxygen–oxygen directions. In other words, the applied pressure will cause a rotation of the oxygen octahedra, resulting in a better exploitation of the empty spaces of the corner-sharing network, in agreement with the experimentally observed phase transition. The high value of the bulk modulus calculated for  $\text{ReO}_3$  can finally be correlated to the high value of the stretching frequency observed experimentally for this material<sup>32</sup> and confirmed in our theoretical study:<sup>4</sup> both observables, in fact, describe the change in energy that accompanies the radial movement of rhenium and oxygen opposed to one another.

#### IV. Structural Deformations: the Role of the Number of Valence Electrons

In the calculations reported in this section, we refer to the optimized cubic structure of  $\text{ReO}_3$  and define  $a_0$  as the calculated equilibrium lattice constant ( $a_0 = 3.71$  Å).

In the study of the lattice deformations we are interested in understanding the different behavior of the three materials and not their absolute properties. For this reason, we do not consider

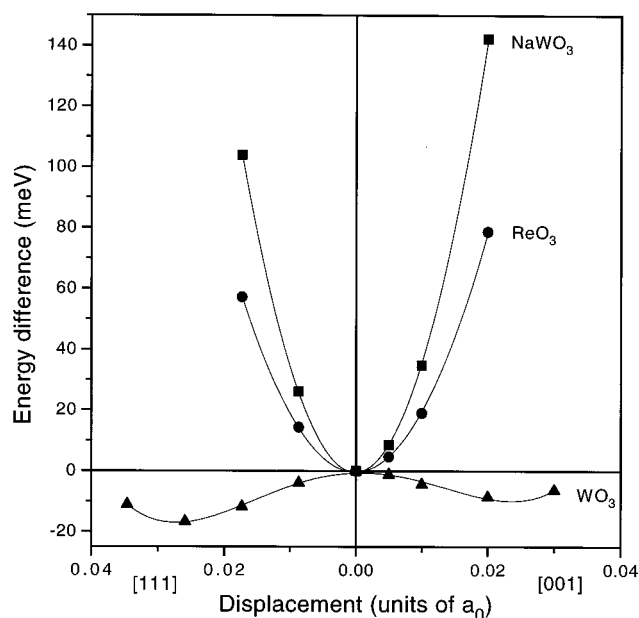


**Figure 6.** Total energy as a function of the transition metal displacement along the [001] (right) and [111] (left) directions for  $\text{ReO}_3$ ,  $\text{NaWO}_3$ , and  $\text{WO}_3$ .

completely optimized structures, but we limit to an idealized description, in which the oxygen sublattice is fixed in its undistorted cubic position. The lattice parameter chosen is  $a_0$  in every case. In our previous work,<sup>4</sup> we have shown that the method we have employed describes with sufficient accuracy the vibrational modes of  $\text{ReO}_3$ . The result not only supports a recent theoretical interpretation of the electrical resistivity of  $\text{ReO}_3$ <sup>33</sup> but also confirms that energy changes following small displacements from the ideal cubic structure are correctly represented. In the present study, we report on ferroelectric displacements of the transition metal along the principal crystallographic directions; results of the deformations are shown in Figure 6, where the total energy is reported for displacements of the transition metal sublattice along the [001] (right panel) and [111] (left panel) crystallographic directions. They correspond to movements of the transition metal ion toward one of its nearest oxygens or toward one face of its coordination octahedron, respectively (see Figure 1). For  $\text{ReO}_3$  and the bronze, the cubic structure remains favored over the distorted ones, and the potential wells have an essentially parabolic shape in the range of deformations examined. In contrast, the cubic structure in  $\text{WO}_3$  is unstable when the transition metal is displaced in both the [001] and [111] directions; the equilibrium position for W is along the [111] direction, and a local minimum exists also in the [001].

Let us now examine the forces acting on the transition metal ion during the displacement: the movement of the metal causes a change in the overlap of its d AOs with the nearest oxygens; as we have illustrated in Section IIIC, this corresponds to a change in the degree of covalence in the metal–oxygen interaction. Moreover, the symmetry reduction that accompanies the metal displacement makes possible the interaction of states that were previously symmetry forbidden. In particular the superdegenerate levels A, B, and 1 are now involved in the metal–oxygen interaction. In Figure 7 we report the projected band structure of distorted  $\text{ReO}_3$ , corresponding to a displacement of the Re sublattice by 3% of the lattice constant  $a_0$  along the [001] direction; the same qualitative effects occur for the other two oxides. Let us now focus on the superdegenerate bands A and 1. In cubic  $\text{ReO}_3$  they correspond to pure  $\text{Re}(t_{2g})$  and pure  $\text{O}(2p)$  states. The transition metal displacement causes an hybridization of the two levels, with bonding character in

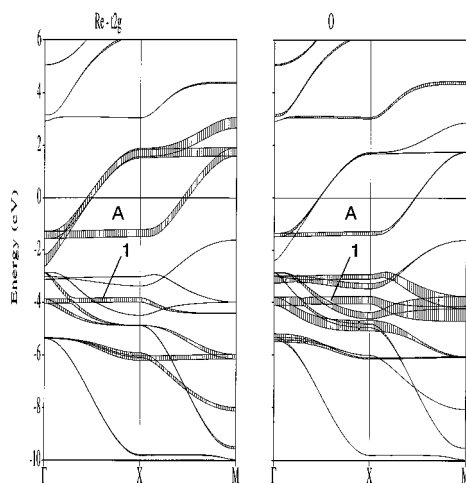


**Figure 7.** Band structure for  $\text{ReO}_3$  after the Re displacement along the [001] direction. Bands A and 1 are the same as in Figure 3; now they have a completely different atomic contribution, showing the effect of the newly formed  $\pi \text{ M}(t_{2g})\text{--O}(2p)$  bond in the distorted structure.

the valence band and antibonding in the conduction band: as a consequence, level A is pushed up by  $\sim 1.0$  eV along the  $\Gamma\text{--X}$  direction; on the other hand, band 1 is stabilized at a lower energy by a similar amount. The onset of the covalent interaction involving bands A and 1 is clearly seen in the projected band structure (Figure 7; compare with Figure 3 for the cubic phase). The comparison of the projected band structures before and after the Re movement unequivocally shows the newly formed  $\pi$  interaction  $\text{O}(2p)\text{--Re}(t_{2g})$ : in the displaced structure, the two superdegenerate bands A and 1 have in fact contributions from both  $\text{Re}(t_{2g})$  and  $\text{O}(2p)$  orbitals. The change affects in different ways the three materials examined: in  $\text{WO}_3$ , only the bonding level 1 is filled and the distortion is energetically stable, while in the metallic oxides  $\text{ReO}_3$  and  $\text{NaWO}_3$  the antibonding orbital is also populated; the antibonding electron destabilizes the distorted structure of the latter materials and opposes to the deformations examined.

The  $e_g$  part of the conduction band (level B) and the  $\text{O}(2p)$  sub-band of  $\sigma$  symmetry are also shifted, though to a minor extent (about 0.2 eV); this confirms that there is a small change in the  $\sigma$  contribution to the bonding. No appreciable change emerges from the band structure projected onto the metal  $e_g$  levels. This analysis is in agreement with the results of HF calculations on  $\text{WO}_3$ ,<sup>2</sup> where we found that the strength of both  $\sigma$  and  $\pi$  interactions changes during the transition metal displacement. In the HF results on  $\text{WO}_3$ , the change in the  $\sigma$  contribution was of higher intensity; for  $\text{ReO}_3$  and  $\text{NaWO}_3$ , however, we also have to account for the depopulation of  $e_g$  levels that we have discussed in the previous section. The  $\sigma$  interactions appear therefore weaker in the two metallic oxides than in  $\text{WO}_3$  both in the cubic phase and during the metal displacement. The same explanation advanced in Section III for the cubic phase applies here during the transition metal displacement.

As we have seen, the metal displacement makes the  $\text{M--O}$  hybridization more effective and originates the bonding and antibonding combinations of levels; the newly formed covalent interaction modifies the band structure (the one-electron energy levels) of the solid in  $k$ -space. From the previous line of arguments, the band structure therefore contains all the relevant information to characterize the covalent  $\text{M--O}$  interaction. The relative stability of the cubic and distorted structures depends critically on the relative population of the bonding and antibonding levels formed upon the transition metal displacement. To complete our analysis of the bonding, we need to examine

in a more extensive way the topic of how the number of valence electrons influences the tendency of these oxides toward symmetry reductions. To evaluate the energy change caused by the rehybridization of levels described above, we have first calculated the one-electron energy  $E_{1e}$  of  $\text{ReO}_3$  before and after the Re displacement. The quantity  $E_{1e}$  can be derived directly from the knowledge of the band structure, by integration over  $k$ -space and energy; although  $E_{1e}$  is only a partial contribution to the total energy, it fully accounts for the energy associated with the electronic degrees of freedom of the system and includes, therefore, the effect on the energy of the electronic rearrangement described above. In the integration, we have used as an intermediate the DOS  $\rho(e)$  (Figure 4) that corresponds to the integral of the band-structure over the whole  $k$ -space.

The number of electrons  $n(e)$  and the one-electron energy per unit cell  $E_{1e}(e)$  are defined as

$$n(e) = \int_{-\infty}^e \rho(\epsilon) d\epsilon \quad (1)$$

$$E_{1e}(e) = \int_{-\infty}^e \epsilon \rho(\epsilon) d\epsilon \quad (2)$$

The true value of the Fermi energy ( $E_f$ ) has been used in the integration and not that employed in Figure 2 (where for graphical convenience we chose  $E_f = 0$ ). We have also shifted the scale of  $n$  in such a way as to have  $n = 0$ , corresponding to a completely filled valence band and empty conduction band. In the new origin,  $n$  equals the number of conduction electrons. In principle, the topology of the band structure (the  $k$ -dependence of energy levels) depends also on the number of electrons ( $n$ ), but comparing the three band structures of Figure 2 it appears reasonable to assume that in the three oxides under investigations the band-structure is rigid as a function of  $n$ . In practice, this means that electrons added to the system simply fill the conduction band, without modifying its topological features in  $k$ -space. Under this assumption,  $\rho(\epsilon)$  does not depend on  $n$ , and combining eqs 1 and 2 we can derive the total one-electron energy of the solid as a function of the number of conduction electrons in the system,  $E_{1e}(n)$ . We calculated the above quantity for cubic  $\text{ReO}_3$  and after the 3%  $a_0$  displacement of Re along the [001] direction. In Figure 8 we plot the difference

$$\Delta_{1e}(n) = E_{1e}^{\text{cub}}(n) - E_{1e}^{[001]}(n) \quad (3)$$

The quantity  $\Delta_{1e}(n)$  gives the energy balance due to the electronic degrees of freedom between the cubic and distorted structures, as a function of  $n$ : when  $\Delta_{1e}(n) > 0$ , the distorted phase is energetically stable with respect to the cubic and vice versa if  $\Delta_{1e}(n) < 0$ . We notice in Figure 8 that for  $n = 0$  (conduction band empty, isoelectronic to  $\text{WO}_3$ ) the distortion has the maximum stability ( $\Delta_{1e}(n=0) = +0.24$  eV). As we have commented above, in this case only the bonding levels in the valence band are filled. By populating the conduction band ( $n > 0$ ), antibonding levels are progressively filled in the distorted structure, and the distortion is gradually destabilized. The two structures are isoenergetical for  $n_0 = 0.98 |e|$  (slightly lower than the actual concentration examined for  $\text{ReO}_3$  and the stoichiometric tungsten bronze). The corresponding quantity in extended Hückel calculations<sup>11</sup> was slightly larger than 1.0  $|e|$ ; the experimental value depends on the system examined, but seems to be lower than 1.0 (see references cited in ref 11). We have shown<sup>2</sup> that the equilibrium configuration in a solid is due to the balance of more forces; in the present case the one-electron levels do not include the complete Coulombic interaction energy (for instance the internuclear terms are excluded from  $E_{1e}$ ). The crystal Coulombic field favors the

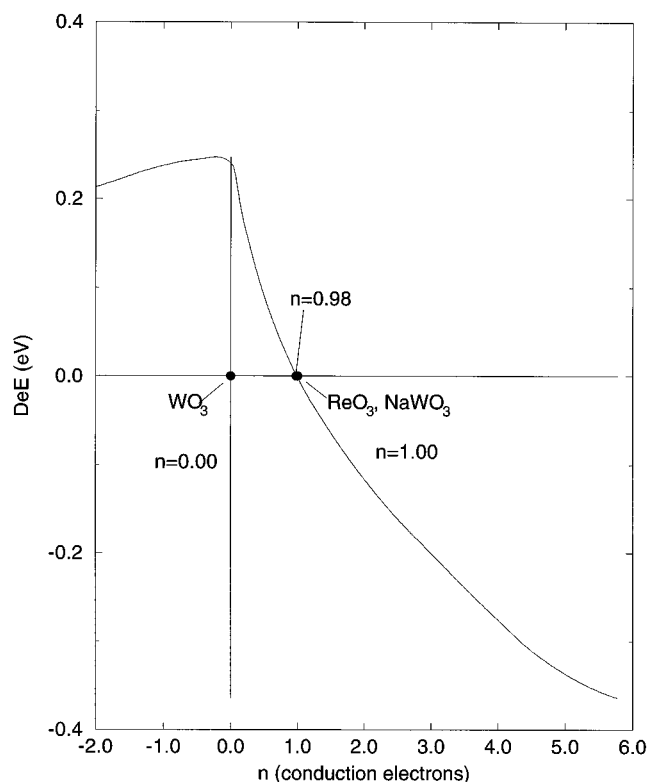


**Figure 8.** Relative stability, in electronvolts, of the cubic with respect to the distorted structure (corresponding to a displacement of the transition metal ion by 3% of the lattice parameter  $a_0$  along the [001] direction) for  $\text{ReO}_3$  as a function of the number of conduction electrons ( $n$ ).

cubic phase and shifts the cubic/distorted equilibrium toward the cubic phase;  $n_0$  is therefore expected to decrease with respect to the value  $n_0 = 0.98$  calculated above. The different intensity of the Coulombic field (the restoring force toward the cubic, highest symmetry structure) explains the different behavior between three- and lower-dimensional structures, as was suggested but not fully accounted for in the extended Hückel calculations.<sup>11</sup>

## V. Summary

We have presented *ab initio* calculations on  $\text{ReO}_3$ ,  $\text{WO}_3$ , and  $\text{NaWO}_3$ . Results compare favorably with those obtained in other quantum-mechanical calculations performed with different Hamiltonians: tight-binding for  $\text{ReO}_3$ , Hartree–Fock for  $\text{ReO}_3$ ,  $\text{WO}_3$ , and  $\text{NaWO}_3$ , atomic sphere approximation DFT for  $\text{NaWO}_3$ .

The differences in the structural behavior between  $\text{WO}_3$  and the metallic compounds  $\text{ReO}_3$  and  $\text{NaWO}_3$  have been analyzed in sections III and IV by performing total-energy calculations. We have shown that the three compounds examined have the same chemical nature but have very pronounced differences in the electric, structural, and mechanical properties. We have also shown the importance of the metal–oxygen hybridization and of the antibonding electron in determining the solid state chemistry of the two metallic oxides.

Energy changes associated with small deformations from the cubic phase have been examined in section IV; they indicate that  $\text{ReO}_3$  and the tungsten bronze are stable when cubic, while off-center displacements of the metal ion are stable in  $\text{WO}_3$ . The different behavior is explained by the destabilization of the conduction band that follows the displacement of the transition metal ion. In  $\text{WO}_3$ , the conduction band is vacant and a stabilization of the valence band favors the distorted structure, while in  $\text{ReO}_3$  and  $\text{NaWO}_3$ , the destabilizing effect

due to the occupation of antibonding levels in the conduction band prevails, opposing the deformations. In addition, our examination of the mechanical properties of the three compounds can provide an explanation for the observed pressure-induced phase transition in  $\text{ReO}_3$ .

To summarize, our calculations provide a detailed explanation of the relation between the electronic and structural properties of perovskite-related compounds.

**Acknowledgment.** F.C. acknowledges financial support from ICI Katalco and Molecular Simulations Inc. (MSI); M.G.S. gratefully acknowledges support (by a grant) from Consejo Nacional de Investigaciones Científicas y Técnicas de la República Argentina and Consejo de Investigaciones de la Universidad Nacional de Rosario.

## References and Notes

- (1) Wyckoff, R. W. G. *Crystal Structures*, 2nd ed.; Interscience: New York, 1965.
- (2) Corà, F.; Patel, A.; Harrison, N. M.; Dovesi, R.; Catlow, C. R. A. *J. Am. Chem. Soc.* **1996**, *118*, 12174.
- (3) Corà, F.; Patel, A.; Harrison, N. M.; Roetti, C.; Catlow, C. R. A. *J. Mater. Chem.* In press.
- (4) Stachiotti, M. G.; Corà, F.; Catlow, C. R. A.; Rodriguez, C. O. *Phys. Rev. B* In press.
- (5) Salje, E. *Acta Crystallogr. B* **1977**, *33*, 547.
- (6) Biltz, W.; Lehrer, G. A.; Meisel, K. *Z. Anorg. Allg. Chem.* **1932**, *207*, 113.
- (7) Razavi, F. S.; Altounian, Z.; Datars, W. R. *Solid State Commun.* **1978**, *28*, 217.
- (8) Axe, J. D.; Fujii, Y.; Batlogg, B.; Greenblatt, M.; Di Gregorio, S. *Phys. Rev. B* **1985**, *31*, 663.
- (9) Jorgensen, J.-E.; Jorgensen, J. D.; Batlogg, B.; Remeika, J. P.; Axe, J. D.; *Phys. Rev. B* **1986**, *33*, 4793.
- (10) Houser, B.; Ingalls, R.; Rehr, J. J. *Physica B* **1995**, *208–209*, 323.
- (11) Wheeler, R. A.; Whangbo, M.-H.; Hughbanks, T.; Hoffmann, R.; Burdett, J. K.; Albright, T. A. *J. Am. Chem. Soc.* **1986**, *108*, 2222.
- (12) Methfessel, M. *Phys. Rev. B* **1988**, *38*, 1537.
- (13) Methfessel, M.; Rodriguez, C. O.; Andersen, O. K. *Phys. Rev. B* **1989**, *40*, 2009.
- (14) Postnikov, A. V.; Neumann, T.; Borstel, G.; Methfessel, M. *Phys. Rev. B* **1993**, *48*, 5910. Postnikov, A. V.; Neumann, T.; Borstel, G. *Phys. Rev. B* **1994**, *50*, 758.
- (15) Perdew, J. P. In *Electronic Structure of Solids*; Ziesche, P., Eschrig, H., Eds.; Akademik Verlag: Berlin, 1991. Perdew, J. P.; Chevary, J. A.; Vosko, S. H.; Jackson, K. A.; Pederson, M. R.; Singh, D. J.; Fiolhais, C. *Phys. Rev. B* **1992**, *46*, 6671.
- (16) Powder Diffraction File, International Centre for Diffraction Data, Sets 27 to 28, 28–1156; p 906.
- (17) Corà, F. Unpublished results.
- (18) Corà, F.; Stachiotti, M. G.; Zicovich-Wilson, C. M.; Cox, P. A.; Catlow, C. R. A. Manuscript in preparation.
- (19) Mattheiss, L. F. *Phys. Rev.* **1969**, *181*, 987.
- (20) Hybertsen, M.; Louie, S. G. *Comments Condens. Matter Phys.* **1987**, *13*, 5.
- (21) Orlando, R.; Dovesi, R.; Roetti, C.; Saunders, V. R. *J. Phys.: Condens. Matter* **1990**, *2*, 7769.
- (22) Granqvist, C. G. *Handbook of Inorganic Electrochromic Materials*; Elsevier: Amsterdam, 1995.
- (23) Christensen, N. E.; Mackintosh, A. R. *Phys. Rev. B* **1987**, *35*, 8246.
- (24) Morinaga, M.; Sato, K.; Harada, J.; Adachi, H.; Ohba, S.; Saito, Y. *J. Phys. C: Solid State Phys.* **1983**, *16*, L177.
- (25) Murnaghan, F. D. *Proc. Natl. Acad. Sci. U.S.A.* **1944**, *30*, 244.
- (26) Birch, F. *J. Geophys. Res.* **1978**, *83*, 1257.
- (27) Davis, L. A.; Gordon, R. B. *J. Chem. Phys.* **1967**, *2250*.
- (28) Bardeen, J. *J. Chem. Phys.* **1938**, *6*, 372.
- (29) Slater, J. C. *Introduction to Chemical Physics*; McGraw-Hill: New York, 1939.
- (30) Vinet, P.; Ferrante, J. H.; Rose, J. H.; Smith, J. R. *J. Geophys. Res.* **1987**, *92*, 9319.
- (31) Brennan, B. J.; Stacey, F. D. *J. Geophys. Res.* **1979**, *84*, 5535.
- (32) Ishii, M.; Tanaka, T.; Akahane, T.; Tsuda, N. *J. Phys. Soc. Jpn.* **1976**, *41*, 908.
- (33) Allen, P. B.; Schulz, W. W. *Phys. Rev. B* **1993**, *47*, 14434.